The Aeronautical Journal (2026), **130**, pp. 464–484
doi:10.1017/aer.2025.10078

RESEARCH ARTICLE

Sparse identification of parafoil dynamics model for path planning

Zhanxin Cui[1,2], Wen Zou[1,3], Zhiwei Feng[2], Qingbin Zhang[2] and Tao Yang[1]

[1]Hypersonic Technology Laboratory, National University of Defense Technology, Changsha, 410073, China
[2]College of Aerospace Science and Engineering, National University of Defense Technology, Changsha, 410073, China
[3]College of Computer, Hunan University of Technology and Business, Changsha, Hunan, Changsha, 410205, China
Corresponding author: Wen Zou; Email: 8320763@qq.com

Received: 6 March 2025; **Revised:** 31 August 2025; **Accepted:** 4 September 2025

Keywords: dynamic models; model reduction; path planning; parafoil system; sparse identification

Abstract

In the field of parafoil airdrop path planning, the inherent complexity and time-sensitive nature of mission requirements necessitate rapid path generation through low-order mathematical models that approximate the system's true dynamics. This study presents a novel sparse identification framework for constructing a parafoil path planning approximate model. Leveraging high-fidelity 9-degree-of-freedom (9 DOF) dynamic simulation data as training inputs, our method identifies simple nonlinear relationships between 3D positional coordinates (for spatial targeting) and yaw angle (for directional control), which are critical path planning parameters. Compared to conventional 4 DOF models, experimental validation using field airdrop data reveals that the proposed sparse model achieves enhanced predictive accuracy while maintaining computational efficiency. Quantitative analysis demonstrates reductions in root mean square error (RMSE) by approximately 12.96% (horizontal position), 54.44% (height) and 37.96% (yaw angle). The efficacy is further confirmed through successful fixed-point homing across diverse initial deployment scenarios, underscoring its potential for parafoil path planning.

Nomenclature

B_e^p	transformation matrix from the earth-fixed reference frame to the canopy reference frame
B_e^c	transformation matrix from the earth-fixed reference frame to the payload reference frame
B_c^p	transformation matrix from the payload reference frame to the canopy reference frame
$E_{3\times3}$	3×3 identity matrix
$0_{3\times3}$	3×3 zero matrix
F_p, M_p	aerodynamic forces and moments at the mass centre of canopy
F_c, M_c	aerodynamic forces and moments at the mass centre of payload
F_{AM}, M_{AM}	forces and moments associated with the added mass
g	gravitational acceleration
I_p, I_c	inertia matrices of the canopy and the payload about the spherical joint
M_a, I_a	mass matrix and inertia matrix associated with the added mass
m_p, m_c	mass of the canopy and the payload
R_p, R_c	position vector matrices from the mass centre of canopy and payload to the spherical joint
$S_e\ (O_eX_eY_eZ_e)$	earth-fixed reference frame
$S_p\ (O_pX_pY_pZ_p)$	canopy reference frame
$S_c\ (O_cX_cY_cZ_c)$	payload reference frame
$S_q\ (O_qX_qY_qZ_q)$	airstream reference frame
V_{ox}, V_{oy}, V_{oz}	components of the velocity of the system mass centre
$X, \dot{X}, U$	data matrices composed of historical data of state variables, state variables derivatives and control inputs under a time series
$\bar{X}, \dot{\bar{X}}$	historical data matrix filtered according to the requirements of parafoil path planning
x_d, y_d, z_d	inertial position of the system mass centre

© The Author(s), 2025. Published by Cambridge University Press on behalf of Royal Aeronautical Society.

https://doi.org/10.1017/aer.2025.10078 Published online by Cambridge University Press

Greek symbol

$\gamma_p, \psi_p, \theta_p$	Euler angles of the canopy (roll, yaw and pitch)
$\gamma_c, \psi_c, \theta_c$	Euler angles of the payload (roll, yaw and pitch)
$\omega_{px}, \omega_{py}, \omega_{pz}$	angular velocity components of the canopy about the spherical joint
$\omega_{cx}, \omega_{cy}, \omega_{cz}$	angular velocity components of the payload about the spherical joint
δ_l, δ_r	trailing edge deflection on the left, right
Θ	library of candidate nonlinear terms
Ξ	sparse coefficient matrix

1.0 Introduction

With the rapid development of aerospace technology, the demand for precise, pinpoint recovery of spacecraft has become increasingly urgent. The successful recovery of SpaceX's fairings, the Genesis reentry capsule and NASA's X-38 project [1, 2] have all validated the feasibility of parafoil spacecraft recovery. Currently, as one of the most effective means of pinpoint airdrop, the parafoil system holds extremely broad prospects for the development in aerospace field [3].

The dynamic model of parafoil system is the basis for studying its flight performance and implementing the path planning. Common parafoil models include the 3 or 4 DOF model [4–6], the 6 DOF model [7], and the 8 [8] or 9 DOF model [9–11], considering the relative motion between the canopy and the payload. Vishnyak [12] proposed a complex 12 DOF model, Yang et al. [13] established a more complex 15 DOF model, and Zhang et al. [14] developed a most complex 18 DOF rigid-body model. In complex airdrop environments, to meet the requirements of rapid flight path design, low-order models are required to approximate the actual motion characteristics of the parafoil.

Current studies in the field of parafoil path planning tend to focus on the overall motion of the parafoil system, ignoring the attitude change and the relative motion between various structures of the system. The most representative approximate model among them is the 4 DOF model, and relevant applications are documented in Li et al. [15, 16]. However, for the particle model obtained based on approximation criteria, the horizontal and vertical directions are decoupled, and the vertical velocity is assumed to be constant. This assumption directly affects the accuracy of the model. Therefore, it is of great practical significance to design an approximate model while ensuring accuracy of model.

Since data-driven methods are gradually on the rise [17], the direct extraction of the dynamic model's structure from data has emerged as one of the approaches for constructing approximate models. Many contemporary machine learning methods (e.g. neural networks, NN) require large-scale datasets for training [18]. However, these techniques exhibit limited generalisation beyond the data collection distribution and struggle to incorporate known physical constraints. This limitation hinders their application in real-time planning and control of strongly nonlinear, high-dimensional, multi-scale pneumatic parafoil systems, as well as online recovery in dynamic, abrupt scenarios. Modern physics-informed hybrid methods, such as physics-informed neural networks (PINNs) [19], provide a powerful framework for embedding physical knowledge. However, even physics-informed data-driven models often lack guarantees of global stability, and the ability of these methods to identify long-term bounded solutions diminishes as the state dimension increases [20]. Gaussian Process Regression (GPR) is highly dependent on kernel function selection, with improper choices potentially leading to underfitting or overfitting [21, 22]. In contrast, the paradigm of parsimonious modeling via sparse identification enables interpretable modeling under data-constrained conditions.

Ever since the onset of the 20th century, scholars have been wholeheartedly dedicated to representing the approximate equations of dynamic systems with a reduced number of relevant terms and discerning the characteristics of dynamic systems from data. Bongard et al. [23] pioneered an automatic methodology for extracting models of nonlinear dynamic systems from experimental data. Schmidt et al. [24] harnessed symbolic regression to identify nonlinear differential equations and put forward a novel approach for establishing the underlying structure of nonlinear dynamic systems and conservation laws

https://doi.org/10.1017/aer.2025.10078 Published online by Cambridge University Press

based on data. Subsequently, Brunton et al. [25, 26] made the first foray into introducing a sparse identification method for nonlinear dynamic systems, namely the Sparse Identification of Nonlinear Dynamics (SINDy). This breakthrough provided an effective solution for discerning the control equations of complex nonlinear systems.

In response to the diverse requirements of different problems, researchers have devised SINDy-based algorithms that are specifically tailored to the research subjects, aiming to surmount the modelling challenges posed by nonlinear systems. For instance, Kaiser et al. [27] ingeniously combined the SINDy with model predictive control (MPC). Chu et al. [28] seamlessly integrated the Lagrangian method and energy-based strategies with the SINDy. Additionally, scholars such as Kaheman [29], Li H. [30, 31], and Li J.C. [32] have also made significant improvements to the SINDy. Numerous innovations expanding the capabilities of the original SINDy algorithm have emerged. For instance, Conti et al. [33] combined autoencoders with SINDy to construct parametric PDEs, enabling efficient continuation of periodic solutions. Specifically, they utilised an autoencoder-SINDy framework [34–36] to identify parameterised dynamics in the latent coordinates of low-dimensional embeddings, facilitating computationally efficient numerical continuation of periodic solutions. In fields such as mechanical systems and fluid mechanics, researchers have begun exploring the integration of machine learning with other numerical methods to enhance predictive performance while preserving model transparency [37]. Moreover, Adaptive Basis Expansion SINDy–a technique merging data-driven and physics-informed modeling–aims to infer the dynamic behaviour of complex systems from limited data samples [38]. In control domains, SINDy-discovered governing equations serve as the basis for the Koopman operator, further enhancing the model's analytical capabilities [39]. At present, the SINDy has achieved remarkable success in a wide array of interdisciplinary fields, including flow field characteristic analysis [40, 41], sensor data identification [42], suspension bridge vibration studies [43] and power system analysis [44].

The SINDy strikes a balance between model complexity and accuracy. A large number of studies have also verified the feasibility of automatically identifying the key parameters of dynamic systems from data. It has brought great inspiration to the construction of approximate models for parafoil systems and provided a new solution for us to establish approximate parafoil models that ensure model accuracy.

Therefore, this paper focuses on the problem of approximate modelling for the parafoil system and conducts research by combining the basic principles of data-driven methods. The structure of this paper is arranged as follows: Section 2 briefly describes the proposed construction strategy for the parafoil approximate model based on sparse identification. Section 3 provides an overview of the high-fidelity 9 DOF parafoil dynamic model established in this study. Section 4 details the sparse identification of the proposed dynamic model, covering aspects such as data collection, construction of the library of candidate nonlinear terms, and solution of the sparse identification matrix. In Section 5, the impact of different training sample sizes on the accuracy of the sparse identification model is analysed. Subsequently, based on experimental data, the computational efficiency and accuracy of the high-fidelity model, the sparse identification model and the 4 DOF dynamic model commonly used in path planning are compared. Finally, Section 6 summarises our main conclusions and offers readers possible future directions for extending work.

2.0 Model construction strategy

In this study, a novel grey-box modelling method is proposed to generate nonlinear models from simulation data. Specifically, the work focuses on the path planning problem of parafoil systems, reveals entirely new nonlinear interaction structures involving 3D positional coordinates, yaw angle, control variables, etc. and successfully constructs an approximate model for parafoil sparse identification.

A schematic diagram of the proposed method is presented in Fig. 1. The specific steps are as follows:

(1) Firstly, considering the high cost and complexity of parafoil test data collection, it is difficult to obtain the training data for the sparse identification model. To solve this problem, a 9 DOF model has been constructed to accurately restore the real-world dynamic characteristics of the

https://doi.org/10.1017/aer.2025.10078 Published online by Cambridge University Press

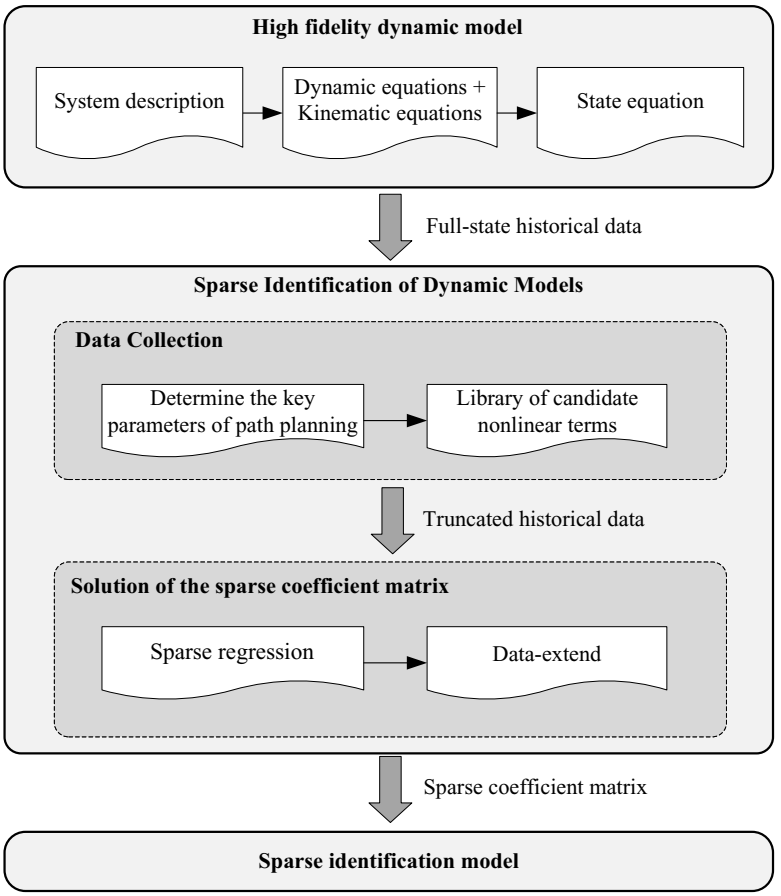


Figure 1. *Construction strategy of the parafoil approximation model.*

parafoil system. By further deriving the state equation from the dynamic equations and kinematic equations, the full-state historical data were obtained, which will be applied to the subsequent sparse identification process of the dynamic model.

(2) Secondly, the sparse identification problem of the dynamic model has been addressed. From the full-state historical data provided by the high-fidelity dynamic model, based on the determined key characteristic parameters, a library of candidate nonlinear terms was constructed and the relevant historical data segments were intercepted.

(3) Finally, by using the constructed library of candidate nonlinear terms and the truncated historical data, the sparse coefficient matrix was solved to obtain the sparse identification model.

3.0 High-fidelity dynamic model

While high-fidelity models (e.g. 12 DOF [12], 15 DOF [13]) capture elastic effects in suspension lines, comparative studies [13] confirm that a simplified 9-DOF rigid-body representation retains sufficient accuracy for trajectory prediction and stability analysis. The rootless multibody dynamics approach was employed for the parafoil system to establish a 9 DOF model, as elaborated by Qin et al. [7] Subsequently, the corresponding state equation was precisely defined. Leveraging this model, high-fidelity simulation datasets were generated. These data served as the fundamental data source that underpinned the subsequent process of sparse identification.

https://doi.org/10.1017/aer.2025.10078 Published online by Cambridge University Press

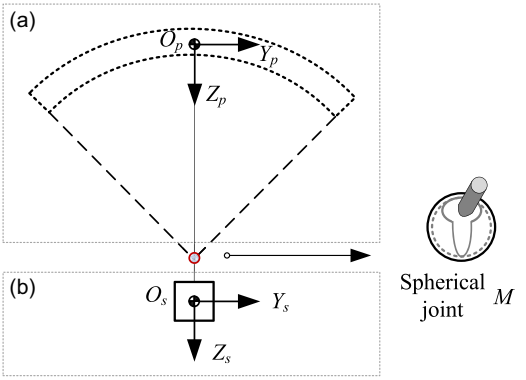


Figure 2. *Two-body parafoil system.*

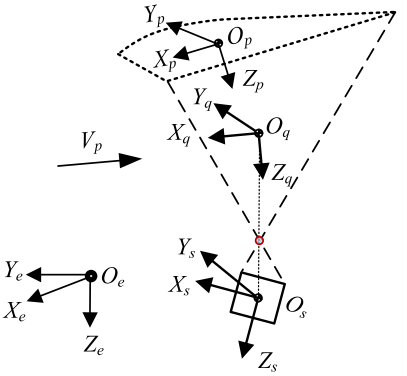


Figure 3. *Reference system.*

3.1 Parafoil system description

After the parafoil is fully inflated, the aerodynamic force is changed by manipulating the deformation of the canopy, thereby achieving flight along a predetermined path. Since the shape of the parafoil does not change significantly, the system can be approximately treated as a two-body rootless system composed of the canopy and payload. Denote the canopy, parachute ropes, etc. as rigid body A, the suspension straps, payload, etc. as rigid body B, and the connecting rope at the intersection point as a spherical joint M. Then the system has a total of nine degrees of freedom, as shown in Fig. 2.

The following reference systems are required in the specific modelling process, as shown in Fig. 3.

(1) **Earth-fixed reference frame** S_e $(O_eX_eY_eZ_e)$.

The origin O_e is at the intended impact point. The O_eZ_e axis is vertically down. The O_eX_e axis lies in the canopy's longitudinal symmetry plane, perpendicular to O_eZ_e, and points toward the East.

(2) **Canopy reference frame** S_p $\left(O_pX_pY_pZ_p\right)$.

The canopy reference system is the body-fixed reference system of the canopy. The origin O_P is at the canopy's mass centre. The O_PX_P axis lies in the canopy's longitudinal symmetry plane, parallel to the canopy's chord length, and points forward. The O_PZ_P axis is also in the longitudinal symmetry plane of the canopy.

(3) **Payload reference frame** S_c $(O_cX_cY_cZ_c)$.

https://doi.org/10.1017/aer.2025.10078 Published online by Cambridge University Press

The payload reference system is the body-fixed reference system of the payload. The origin O_c is at the payload's mass centre. The O_cX_c axis is parallel to the payload's central axis and points forward of the parafoil system. The O_cZ_c axis lies in the payload's longitudinal symmetry plane.

(4) **Airstream reference frame** $S_q\left(O_qX_qY_qZ_q\right)$.

The origin O_q is at the parafoil system mass centre. The O_QX_Q axis is opposite the oncoming flow. The O_QZ_Q axis lies in the parafoil system longitudinal symmetry plane, perpendicular to O_QX_Q, and points down.

3.2 Dynamics and kinematics equations

To facilitate the design of the parafoil path planning, the Lagrange equations in the form of quasi-coordinates are adopted for dynamic modelling. For the parafoil system shown in Fig. 2, the position components x_e, y_e and z_e of the position vector in the earth-fixed reference frame, the Euler angles γ_p, ψ_p and θ_p of the canopy, as well as the Euler angles γ_c, ψ_c and θ_c of the payload are set as the quasi-coordinates of the parafoil system.

The velocity components v_x, v_y and v_z of the mass centre velocity vector of the system in S_e $(O_eX_eY_eZ_e)$, the angular velocity components ω_{px}, ω_{py} and ω_{pz} of the canopy, and the angular velocity components ω_{cx}, ω_{cy} and ω_{cz} of the payload are taken as the quasi-velocities.

With the quasi-coordinates and quasi-velocities defined, the matrix-form representation can now be derived, as shown in Equations (1) and (2).

$$\boldsymbol{q}=\begin{bmatrix}\boldsymbol{R} & \boldsymbol{E}_c & \boldsymbol{E}_p\end{bmatrix}^{\mathrm{T}},\ \boldsymbol{v}=\begin{bmatrix}\boldsymbol{V}_o & \boldsymbol{\omega}_c & \boldsymbol{\omega}_p\end{bmatrix}^{\mathrm{T}}, \tag{1}$$

where,

$$\begin{cases}\boldsymbol{R}=\begin{bmatrix}x_e & y_e & z_e\end{bmatrix}^{\mathrm{T}}\\ \boldsymbol{V}_o=\begin{bmatrix}V_{ox} & V_{oy} & V_{oz}\end{bmatrix}^{\mathrm{T}}\\ \boldsymbol{E}_p=\begin{bmatrix}\gamma_p & \psi_p & \theta_p\end{bmatrix}^{\mathrm{T}}\\ \boldsymbol{\omega}_p=\begin{bmatrix}\omega_{px} & \omega_{py} & \omega_{pz}\end{bmatrix}^{\mathrm{T}}.\\ \boldsymbol{E}_c=\begin{bmatrix}\gamma & \psi_c & \theta_c\end{bmatrix}^{\mathrm{T}}\\ \boldsymbol{\omega}_c=\begin{bmatrix}\omega_{cx} & \omega_{cy} & \omega_{cz}\end{bmatrix}^{\mathrm{T}}\end{cases} \tag{2}$$

The multi-body dynamics method is adopted to conduct parafoil modelling. The detailed derivation process is available in Zhang et al. [14], where relevant steps and explanations are presented for further exploration. By integrating the kinematic and dynamic relationships, the Lagrange equations are established as shown in Equation (3).

$$\begin{cases}\dot{\boldsymbol{q}}=\boldsymbol{B}\boldsymbol{v}\\ \boldsymbol{M}\left(\boldsymbol{q}\right)\dot{\boldsymbol{v}}=\boldsymbol{F},\end{cases} \tag{3}$$

the state transition matrix $\boldsymbol{B}$ is expressed as follows,

$$\boldsymbol{B}=diag\left(\boldsymbol{E}_{3\times3}^{\mathrm{T}} \quad \boldsymbol{D}_c^{-1} \quad \boldsymbol{D}_p^{-1}\right). \tag{4}$$

$$\boldsymbol{D}_c=\begin{bmatrix}1 & -\tan\theta_c\cos\gamma_c & \tan\theta_c\sin\gamma_c\\ 0 & \cos\gamma_c/\cos\theta_c & -\sin\gamma_c/\cos\theta_c\\ 0 & \sin\gamma_c & \cos\gamma_c\end{bmatrix}, \tag{5}$$

$$\boldsymbol{D}_p=\begin{bmatrix}1 & -\tan\theta_p\cos\gamma_p & \tan\theta_p\sin\gamma_p\\ 0 & \cos\gamma_p/\cos\theta_p & -\sin\gamma_p/\cos\theta_p\\ 0 & \sin\gamma_p & \cos\gamma_p\end{bmatrix}, \tag{6}$$

https://doi.org/10.1017/aer.2025.10078 Published online by Cambridge University Press

the generalised mass matrix $\boldsymbol{M}$ is expressed as follows,

$$\boldsymbol{M}=\begin{bmatrix}(m_p+m_c)\boldsymbol{E}_{3\times3}+\boldsymbol{M}_a & -\boldsymbol{B}_c^p m_c\tilde{\boldsymbol{R}}_c & -(m_p\boldsymbol{E}_{3\times3}+\boldsymbol{M}_a)\tilde{\boldsymbol{R}}_p\\ m_c\tilde{\boldsymbol{R}}_c & \boldsymbol{I}_c & 0_{3\times3}\\ -(m_p\boldsymbol{E}_{3\times3}+\boldsymbol{M}_a)\tilde{\boldsymbol{R}}_p & 0_{3\times3} & \boldsymbol{I}_p+\boldsymbol{I}_a\end{bmatrix}, \tag{7}$$

the generalised force matrix $\boldsymbol{F}$ is expressed as follows,

$$\begin{aligned}\boldsymbol{F}=&\begin{bmatrix}-(m_c+m_p)\boldsymbol{E}_{3\times3}\left(\tilde{\boldsymbol{\omega}}_p\boldsymbol{B}_d^p\boldsymbol{V}_o\right)\\ -\tilde{\boldsymbol{\omega}}_c\left(\boldsymbol{I}_c\boldsymbol{\omega}_c\right)-m_c\boldsymbol{R}_c\left(\tilde{\boldsymbol{\omega}}_c\boldsymbol{B}_d^c\boldsymbol{V}_o\right)\\ -\tilde{\boldsymbol{\omega}}_p\left(\boldsymbol{I}_p\boldsymbol{\omega}_p\right)-m_p\tilde{\boldsymbol{R}}_p\left(\tilde{\boldsymbol{\omega}}_p\boldsymbol{B}_d^p\boldsymbol{V}_o\right)\end{bmatrix}+\begin{bmatrix}m_c\boldsymbol{g}+m_p\boldsymbol{g}\\ \tilde{\boldsymbol{R}}_c\left(m_c\boldsymbol{g}\right)\\ \tilde{\boldsymbol{R}}_p\left(m_p\boldsymbol{g}\right)\end{bmatrix}\\ &+\begin{bmatrix}\boldsymbol{F}_p+\boldsymbol{B}_c^p\boldsymbol{F}_c+\boldsymbol{F}_{AM}\\ \boldsymbol{M}_c\\ \boldsymbol{M}_p+\boldsymbol{M}_{AM}\end{bmatrix}-\begin{bmatrix}m_c\boldsymbol{B}_c^p\left[\tilde{\boldsymbol{R}}_c\left(\tilde{\boldsymbol{\omega}}_c\boldsymbol{\omega}_c\right)\right]+m_p\left[\tilde{\boldsymbol{R}}_p\left(\tilde{\boldsymbol{\omega}}_p\boldsymbol{\omega}_p\right)\right]\\ 0_{3\times3}\\ 0_{3\times3}\end{bmatrix},\end{aligned} \tag{8}$$

The symbols in this equation are defined in Equations (7) and (8) as follows: Transformation matrices include $\boldsymbol{B}_e^p$ (from earth-fixed to canopy frame), $\boldsymbol{B}_e^c$ (from earth-fixed to payload frame), and $\boldsymbol{B}_c^p$ (from payload to canopy frame). Matrix notations comprise $\boldsymbol{E}_{3\times3}$ (3×3 identity matrix) and $0_{3\times3}$ (3×3 zero matrix). Mass properties are m_p (canopy mass) and m_c (payload mass), while $\boldsymbol{I}_p$ and $\boldsymbol{I}_c$ are inertia matrices about the spherical joint. Position vectors $\boldsymbol{R}_p$ and $\boldsymbol{R}_c$ extend from the canopy and payload mass centres to the spherical joint, respectively. Aerodynamic forces and moments are $\boldsymbol{F}_p, \boldsymbol{M}_p$ (at canopy mass centre) and $\boldsymbol{F}_c, \boldsymbol{M}_c$ (at payload mass centre), with $\boldsymbol{F}_{AM}, \boldsymbol{M}_{AM}$ representing added mass effects governed by $\boldsymbol{M}_a$ (added mass matrix) and $\boldsymbol{I}_a$ (added inertia matrix). $\boldsymbol{V}_{ox}, \boldsymbol{V}_{oy}, \boldsymbol{V}_{oz}$ are velocity components of mass centre.

3.3 State equation

From Equations (1) to (8), the complete expression of the dynamic and kinematic equations for the parafoil system has been derived. To conduct the sparse identification of the system more conveniently, the model is further transformed into a nonlinear state equation suitable for the design of the control system, and the system state variables are defined as follows,

$$\boldsymbol{x}=\begin{bmatrix}\boldsymbol{q} & \boldsymbol{v}\end{bmatrix}^{\mathrm{T}}, \tag{9}$$

define δ_l and δ_r as the trailing edges deflection on the left and right of parafoil, which are used as the control inputs and expressed as,

$$\boldsymbol{u}=\begin{bmatrix}\delta_l & \delta_r\end{bmatrix}^T, \tag{10}$$

subsequently, the state equations are obtained as follows,

$$\frac{\mathrm{d}}{\mathrm{d}t}\boldsymbol{x}=f(\boldsymbol{x},\boldsymbol{u}), \tag{11}$$

For the parafoil dynamic model, Equation (11) can be expressed in matrix form as,

$$\begin{bmatrix}\dot{x}_1(t)\\ \dot{x}_2(t)\\ \vdots\\ \dot{x}_{18}(t)\end{bmatrix}=\begin{bmatrix}f_1(\boldsymbol{x},\boldsymbol{u})\\ f_2(\boldsymbol{x},\boldsymbol{u})\\ \vdots\\ f_{18}(\boldsymbol{x},\boldsymbol{u})\end{bmatrix}, \tag{12}$$

where $x_1 \sim x_{18}$ correspond to the 18 state parameters at time t in Equation (2). Given the initial state quantities and control inputs, the motion characteristics of the two-body parafoil system can be obtained via numerical integration methods.

https://doi.org/10.1017/aer.2025.10078 Published online by Cambridge University Press

4.0 Sparse identification of dynamic models

Leveraging the high-fidelity simulation data generated by the 9 DOF dynamic model of the parafoil system, the sparse identification method for nonlinear dynamics with control is adopted. This method is used to accurately identify the nonlinear structure and key parameters of the dynamic system from the data, ultimately constructing a dynamic model specifically tailored for path planning.

4.1 Data collection

1. Full-state historical data
   Collect the data of the control input, state variables and their derivatives in the time series of the 9 DOF dynamic model of the parafoil system in the simulation and build a historical dataset. These data are arranged according to the state variables to form three data matrices [9], X, $\dot{X}$ and U, as shown in Equation (13).

$$\begin{cases} X = \begin{bmatrix} \boldsymbol{x}(t_1) & \boldsymbol{x}(t_2) & \cdots & \boldsymbol{x}(t_m) \end{bmatrix} \in \mathbb{R}^{18\times m} \\ \dot{X} = \begin{bmatrix} \dot{\boldsymbol{x}}(t_1) & \dot{\boldsymbol{x}}(t_2) & \cdots & \dot{\boldsymbol{x}}(t_m) \end{bmatrix} \in \mathbb{R}^{18\times m}, \\ U = \begin{bmatrix} \boldsymbol{u}(t_1) & \boldsymbol{u}(t_2) & \cdots & \boldsymbol{u}(t_m) \end{bmatrix} \in \mathbb{R}^{2\times m} \end{cases} \tag{13}$$

2. Determining key parameters for parafoil path planning
   According to the experience of engineering applications [45], for the path planning of the parafoil system, only a few nonlinear terms are crucial, such as the state variables x_d, y_d, z_d, ψ_p and the left and right trailing edge deflections δ_l and δ_r. While roll dynamics significantly affect turning performance, the yaw state serves as an adequate descriptor for autonomous lateral path planning under steady-flight conditions. This simplification aligns with the 4 DOF modeling conventions for large parafoils and prioritises real-time computational efficiency.

   Library terms are pruned based on their physical interpretability in parafoil dynamics. For example, cross-terms like $\delta_l \cdot \psi_p$ have no direct correspondence in force/moment equations, while their effects are implicitly encapsulated by state variables ψ_p. A few other terms can be regarded as zero terms. Therefore, the function $f(\boldsymbol{x}, \boldsymbol{u})$ on the right-hand side of Equation (12) can be sparsely represented in a high dimensional nonlinear function space.

3. Truncation of historical data
   The 1st, 2nd, 3rd and 8th rows of the corresponding historical data matrices X and $\dot{X}$ are extracted to form new data matrices $\bar{X}$ and $\dot{\bar{X}}$. When all data under the time series $\{t_1, t_2, \cdots, t_m\}$ are expanded, the matrices can be obtained in Equations (14) to (16).

$$\bar{X} = \begin{bmatrix} x_d(t_1) & x_d(t_2) & \cdots & x_d(t_m) \\ y_d(t_1) & y_d(t_2) & \cdots & y_d(t_m) \\ z_d(t_1) & z_d(t_2) & \cdots & z_d(t_m) \\ \psi_p(t_1) & \psi_p(t_2) & \cdots & \psi_p(t_m) \end{bmatrix}, \tag{14}$$

$$\dot{\bar{X}} = \begin{bmatrix} \dot{x}(t_1) & \dot{x}_d(t_2) & \cdots & \dot{}_d(t_m) \\ \dot{y}_d(t_1) & \dot{y}_d(t_2) & \cdots & \dot{y}_d(t_m) \\ \dot{z}_d(t_1) & \dot{z}_d(t_2) & \cdots & \dot{z}_d(t_m) \\ \dot{\psi}_p(t_1) & \dot{\psi}_p(t_2) & \cdots & \dot{\psi}_p(t_m) \end{bmatrix}, \tag{15}$$

$$U = \begin{bmatrix} \delta_l(t_1) & \delta_l(t_2) & \cdots & \delta_l(t_m) \\ \delta_r(t_1) & \delta_r(t_2) & \cdots & \delta_r(t_m) \end{bmatrix}. \tag{16}$$

https://doi.org/10.1017/aer.2025.10078 Published online by Cambridge University Press

4. Library of candidate nonlinear terms
Combined with the sparsity analysis, by introducing the sparse coefficient Ξ and library of candidate nonlinear terms Θ, the dynamic equation of the parafoil can be expressed as Equations 17,

$$\dot{\bar{X}} = \Xi\Theta^T(\bar{X}, U), \tag{17}$$

where Θ is composed of simple combinations of certain items from the state variable data matrix $\bar{X}$ and the control input data matrix U.

In this paper, only closely related combination terms are set for the parafoil system to obtain the library of candidate nonlinear terms. When the terms in the library are expanded according to the time series $\{t_1, t_2, \cdots, t_m\}$, it can be expressed as Equation (18):

$$\Theta^T(\bar{X}, U) = \begin{bmatrix} 1 & \cdots & 1 \\ x_d(t_1) & \cdots & x_d(t_m) \\ y_d(t_1) & \cdots & y_d(t_m) \\ z_d(t_1) & \cdots & z_d(t_m) \\ \psi_p(t_1) & \cdots & \psi_p(t_m) \\ \cos(\psi_p)(t_1) & \cdots & \cos(\psi_p)(t_m) \\ \sin(\psi_p)(t_1) & \cdots & \sin(\psi_p)(t_m) \\ \delta_l(t_1) & \cdots & \delta_l(t_m) \\ \delta_r(t_1) & \cdots & \delta_r(t_m) \end{bmatrix}, \tag{18}$$

Based on the above conditions, the corresponding sparse coefficient matrix is a 4×9 matrix, and its representation form is as Equation (19):

$$\Xi = [\xi_1\ \xi_2\ \xi_3\ \xi_4]^{\mathrm{T}} \in \mathbb{R}^{4\times 9}. \tag{19}$$

4.2 Solution of the sparse coefficient matrix

4.2.1 Sparse coefficient estimation via LASSO-regularised regression

Based on the historical data and the library of candidate nonlinear terms, the sparse coefficient matrix Ξ can be obtained via sparse regression. Some coefficients in the matrix Ξ are shrunk to zero to reduce the model complexity, thereby achieving the purpose of feature selection.

The basic idea of Least Absolute Shrinkage and Selection Operator (LASSO) regression is adopted to approximate and solve the sparse coefficients, as shown in Equation (20). LASSO is a linear regression algorithm used for feature selection and model regularisation. It constrains the coefficients in the model by applying the LASSO penalty and shrinks some coefficients to zero. The LASSO regression equation is used to identify the sparse matrix with the best model performance in the library of candidate nonlinear terms,

$$\xi_k = \underset{\xi_k}{\operatorname{argmin}} \left\| \dot{\bar{X}}_k - \xi_k \Theta^T(\bar{X}, U) \right\|_2^2 + \lambda \|\xi_k\|_1, \tag{20}$$

where $\dot{\bar{X}}_k$ represents the k-th row of $\dot{\bar{X}}$ ($k = 1, 2, 3, 4$), ξ_k represents the k-th row of Ξ and λ is the weight term for controlling the sparsity adjustment.

Combining the summaries in Section 4.1, the basic principle of the sparse identification of the parafoil system can be obtained, as shown in Fig. 4. Here, the solid dots represent the coefficients corresponding to the key terms selected by the sparse identification, and the hollow dots represent the zero terms.

4.2.2. Expanding historical data quantity

In this section, a method for solving the sparse matrix of the parafoil with data expansion is proposed to improve the accuracy of the sparse identification model and expand the amount of historical data.

https://doi.org/10.1017/aer.2025.10078 Published online by Cambridge University Press

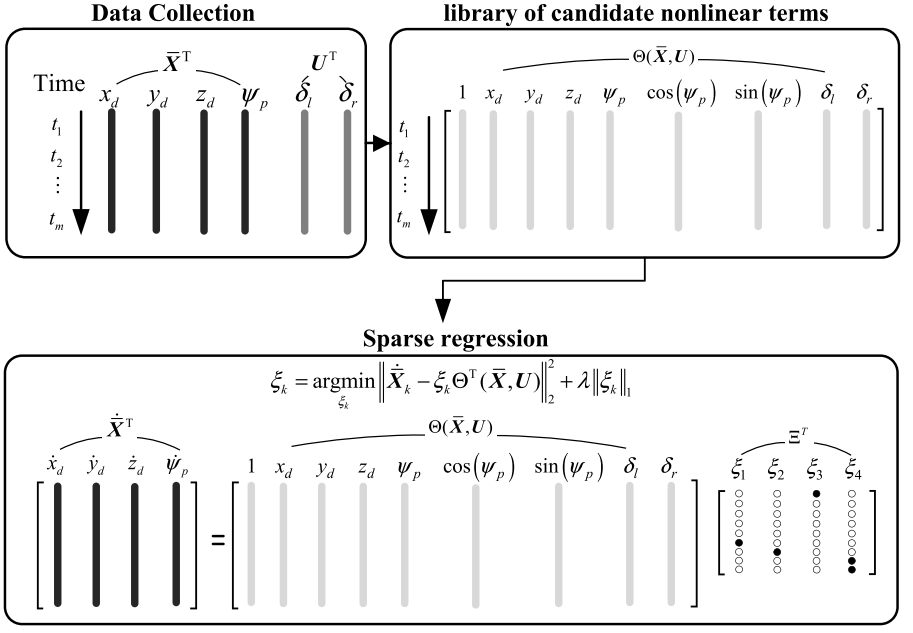


Figure 4. *Principles of sparse identification for parafoil systems.*

Randomly set the initial values of the state variables and control inputs for P groups (training sample sizes). Perform simulations using the high-fidelity 9 DOF dynamic model established in Section 3. After data organisation, P groups of data matrices $\bar{X}$, $\dot{\bar{X}}$, and U are obtained.

Then the generalised model shown in Equation (17) can be expanded and expressed as Equation (21). The expression of the block matrix can be systematically derived by drawing on the definitions of the library of candidate nonlinear terms and the sparse coefficient matrix, as shown in Equation (22).

$$\begin{cases} \dot{\bar{X}}^{(1)} = \Xi\Theta^T(\bar{X}^{(1)}, U^{(1)}) \\ \dot{\bar{X}}^{(2)} = \Xi\Theta^T(\bar{X}^{(2)}, U^{(2)}), \\ \cdots \\ \dot{\bar{X}}^{(P)} = \Xi\Theta^T(\bar{X}^{(P)}, U^{(P)}) \end{cases} \tag{21}$$

$$\begin{bmatrix} \dot{\bar{X}}^{(1)} \\ \dot{\bar{X}}^{(2)} \\ \cdots \\ \dot{\bar{X}}^{(P)} \end{bmatrix} = \Xi \begin{bmatrix} \Theta^T(\bar{X}^{(1)}, U^{(1)}) \\ \Theta^T(\bar{X}^{(2)}, U^{(2)}) \\ \cdots \\ \Theta^T(\bar{X}^{(P)}, U^{(P)}) \end{bmatrix}, \tag{22}$$

The left-hand side of the equation is arranged into the matrix $\dot{\bar{X}}_E$, and the right-hand side is arranged into the product of the sparse coefficient matrix and the matrix $(\Theta_E)^{\mathrm{T}}$, thereby obtaining the expression of the sparse coefficient matrix of the parafoil with data expansion, which corresponds to Equation (23).

$$\Xi = \dot{\bar{X}}_E\left((\Theta_E)^T\right)^+, \tag{23}$$

the symbol "+" denotes the pseudo-inverse of a matrix.

By integrating the method elaborated in Section 4.2.1, the LASSO regression is employed to derive the sparse coefficient matrix Ξ. Then, an algorithm for solving the sparse coefficient matrix of the parafoil with data expansion is formulated. The specific details are presented in Algorithm 1.

https://doi.org/10.1017/aer.2025.10078 Published online by Cambridge University Press

Algorithm 1: Parafoil sparse coefficient matrix solution algorithm

Input: The extended time derivative matrix $\bar{X}_E$, the extended library of candidate nonlinear terms Θ_E, the number ofi terative optimizations N, the range of regularization parameters $\lambda_{range} = [\lambda_{min}, \lambda_{max}]$, the number of λ uniformly distributed in the logarithmic space λ_{num}, the number off olds in cross - validation K_{Fold}

Output: The sparse coefficient matrix Ξ, Optimal regularization parameter vector $\lambda_{optimal}$

Function SINDY-Parafoil($\dot{\bar{X}}_E$,Θ_E,N,λ_{range},λ_{num},K_{Fold})
  $\Xi \leftarrow$ zeros (N, size (Θ_E, 2));
  $\lambda_{optimal} \leftarrow$ zeros (1, N);
  $\lambda_{grid} \leftarrow$ logspace($\log_{10}(\lambda_{min})$, $\log_{10}(\lambda_{max})$, λ_{num}); // Prepare lambda grid
  for $i \leftarrow 1$ **to** N **do**
    $cv \leftarrow$ cvpartition (size (Θ_E), 1), 'KFold', K_{Fold});
    $MSE_{values} \leftarrow$ zeros (λ_{num}, 1);
    // K - fold cross - validation initialization
    for $j \leftarrow 1$ **to** λ_{num} **do**
      $\lambda \leftarrow \lambda_{grid}(j)$;
      $MSE_{fold} \leftarrow$ zeros (K_{Fold}, 1);
      for $k \leftarrow 1$ **to** K_{Fold} **do**
        $train_{Idx} \leftarrow$ training (cv, k);
        $test_{Idx} \leftarrow$ test (cv, k); // Divide the training set and validation set
        $\xi \leftarrow$ lasso($\Theta_E(train_{Idx}, :)$, $\dot{\bar{X}}_E(train_{Idx})$, 'Lambda', λ); // Train the Lasso model
        $\dot{\bar{X}}_{E_{pred}} \leftarrow \Theta_E(train_{Idx}, :)\ \xi$; // Validation set prediction
        $MSE_{fold}(k) \leftarrow$ mean(($\dot{\bar{X}}_E(train_{Idx})$ - $\dot{\bar{X}}_{E_{pred}}$).^{2});
      end
      $MSE_{values}(i) \leftarrow$ mean(MSE_{fold}); // Calculate the average MSE
    end
    [, min_{idx}] $\leftarrow$ min(MSE_{values});
    $\lambda_{opt} \leftarrow \lambda_{grid}(min_{idx})$;
    $\xi \leftarrow$ lasso(Θ_E, $\dot{\bar{X}}_E(:, i)$, 'Lambda', λ_{opt}); // Optimize lambda and train the final model on the entire dataset
    Ξ(:, ind) $\leftarrow \xi$;
    $\lambda_{optimal} \leftarrow \lambda_{opt}$;
  end
  $\Xi(abs(\Xi) < 10^{-6}) \leftarrow 0$; // Post - processing: Remove extremely small coefficients
end Function

This paper employs 10-fold cross-validation to search for the optimal regularisation parameter λ in logarithmic space: 100 logarithmically spaced candidate values are generated within $[10^{-6}, 10]$. The dataset is randomly partitioned into 10 subsets. For each candidate λ, the LASSO model is trained on nine subsets, and the prediction Mean Squared Error (MSE) is computed on the remaining subset. The λ that minimises the average MSE is selected. This process is optimised independently per state dimension to adapt to varying sparsity requirements of the dynamics. A post-processing step truncates sparse regression coefficients with absolute values below 10^{-6} to zero, eliminating numerical noise-induced perturbations and enhancing model stability and interpretability.

5.0 Simulation

In this section, the performance of the sparse identification model is mainly evaluated. Firstly, the relationship between different training sample sizes and the accuracy of the sparse identification model is

https://doi.org/10.1017/aer.2025.10078 Published online by Cambridge University Press

Table 1. *The main parameters of parafoil system*

Parameters	Values
Span [m]	18.5
Chord [m]	7.5
Canopy mass [kg]	220
Payload mass [kg]	4500

Table 2. *Initial simulation condition of parafoil system*

Parameters	Values
Deployment height [m]	1,800
Initial horizontal velocity [m/s]	28
Vertical velocity [m/s]	10.8

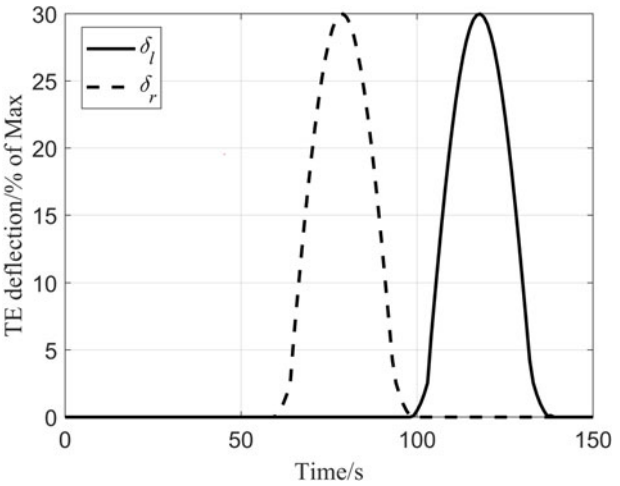


Figure 5. *Trailing edge deflection on the left/right of parafoil.*

examined in detail. Secondly, leveraging experimental data, this study comprehensively evaluates both computational efficiency and accuracy. It conducts a detailed comparison among the high-fidelity model, the sparse-identification model, and the widely used 4-DOF dynamic model in path planning, highlighting their respective advantages and limitations. Finally, the applicability of the sparse identification model in path planning scenarios is analysed.

5.1 Influence of training sample sizes

The mechanism by which the amount of data affects the accuracy of the sparse identification model is determined by taking the parafoil system shown in Table 1 as an example and conducting an error analysis. In line with the process depicted in Fig. 4 and Algorithm 1, the number of groups P of state variables and control inputs is set to 1, 10, 100 and 1,000 respectively. As a result, four approximate sparse identification models with different data volumes are obtained. Under the same simulation conditions, the differences between the high-fidelity model and the four sparse identification models are compared. The initial simulation conditions are set according to the experiments, as detailed in Table 2, and the control variables are shown in Fig. 5.

https://doi.org/10.1017/aer.2025.10078 Published online by Cambridge University Press

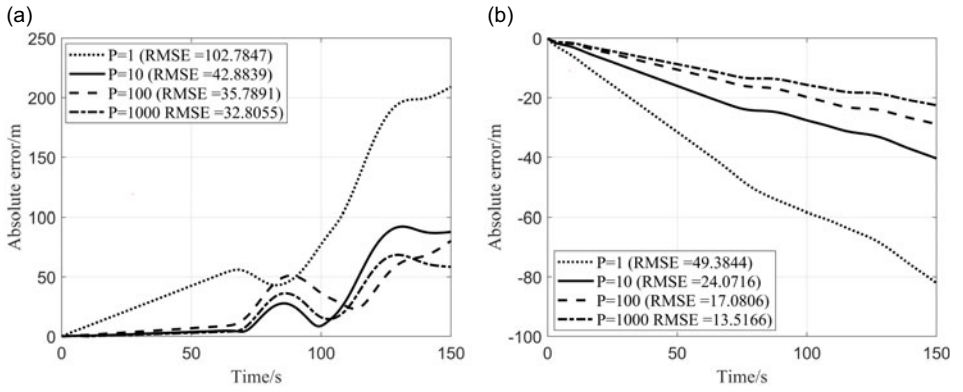


Figure 6. *Error analysis of displacement.*

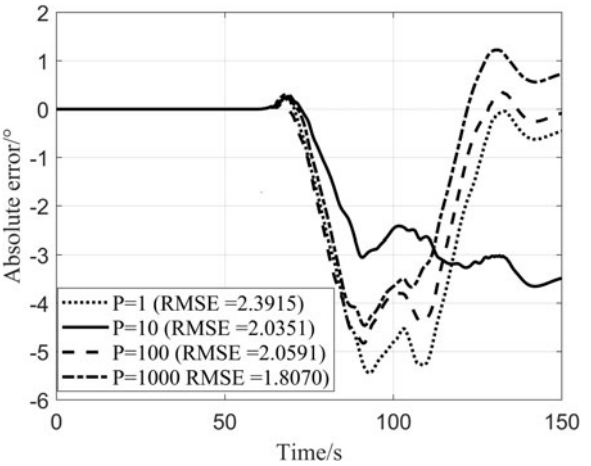


Figure 7. *Error analysis of yaw angle.*

It is worth noting that the parameters of the parafoil system used for training the model and validation remain consistent. However, to ensure generalisation ability, we implemented a strict data separation strategy: for training data, randomly generated initial states and control inputs are used; for testing, completely independent initial states (Table 2) are adopted, the control inputs are smooth (Fig. 5), and the samples that do not completely overlap with the training set are included.

Eventually, the comparison curves for the horizontal and vertical displacements, as well as the yaw angle, are acquired and shown in Figs 6 and 7. Analysis shows that:

(1) As the simulation time progresses, the error in the horizontal displacement gradually accumulates, manifesting a tendency of fluctuating growth. With the continuous increase in the groups P of the initial random state variables, the corresponding RMSE of the horizontal displacement steadily diminishes. When P reaches 1,000, the RMSE attains its minimum value.

(2) The error in the vertical displacement demonstrates a linearly ascending trend as the simulation time lengthens. Moreover, subsequent to an increase in P, the RMSE gradually drops.

(3) The error in the yaw angle decreases concomitantly with the increase in the groups P, and the RMSE also gradually decreases.

https://doi.org/10.1017/aer.2025.10078 Published online by Cambridge University Press

In summary, a preliminary conclusion can be derived: the initial data volume exerts a significant influence on the accuracy of the sparse identification model. Specifically, the greater the data volume, the higher the accuracy. Nevertheless, it is evident that an augmentation in the data volume will inevitably lead to an increase in computational time consumption. Consequently, in practical applications, it is necessary to carefully consider and strike a balance between the model accuracy and the available computational resources.

In the subsequent analysis, the number of groups P of random state variables is set to 1,000, and the sparse coefficient matrix of the key parameters of the parafoil system is obtained in Equation (24),

$$\Xi^T = \begin{bmatrix} \xi_1 & \xi_2 & \xi_3 & \xi_4 \end{bmatrix} = \begin{bmatrix} -0.141 & -0.060 & 10.858 & 0 \\ 0 & 0 & 0 & 0 \\ 0 & 0 & 0 & 0 \\ 0 & 0 & 0 & 0 \\ 0 & 0 & 0 & 0 \\ 28.05 & -0.149 & -0.014 & 0 \\ 0.0560 & 28.05 & 0.015 & 0 \\ 0 & 0 & 0 & 0.14 \\ 0.081 & -0.068 & -0.014 & -0.14 \end{bmatrix}. \tag{24}$$

Combined with Equation (24), the sparse identification model of the parafoil system is constructed. This model is completely data-driven, and its parameters are directly obtained through model reduction. Its form is as Equation (25):

$$\begin{cases} \dot{x}_d = \Theta(\bar{X}, U)\xi_1 \\ \dot{y}_d = \Theta(\bar{X}, U)\xi_2 \\ \dot{z}_d = \Theta(\bar{X}, U)\xi_3 \\ \dot{\psi}_p = \Theta(\bar{X}, U)\xi_4 \end{cases}. \tag{25}$$

5.2 Model performance comparison

In the real implementation of path planning, the model selection process is multifaceted. It requires a comprehensive consideration of the model's prediction accuracy for the parafoil's path and its computational efficiency. Additionally, the running time of each model is a crucial determinant. This holistic approach empowers decision makers to make more informed choices when selecting the most suitable model for specific path planning. By doing so, the goal is to ensure that the selected model attains optimal performance, striking an effective balance between high-precision prediction accuracy and efficient computational resource utilisation. The primary objective of this section is to evaluate the single simulation running time and position prediction capabilities of three distinct models: the high-fidelity model, the sparse identification model and the 4 DOF dynamic model (which is prevalently employed in path planning for the parafoil system).

5.2.1 Computational efficiency evaluation

Firstly, 1,000 computer simulations were conducted to compare the simulation times for the three models, as presented in Fig. 8. The analysis reveals that the running time of the high-fidelity model is approximately 0.053 s, while those of the sparse identification model and the 4 DOF dynamic model are around 0.0015 s and about 0.0014 s. The performance disparities are remarkable. Evidently, the running time of the high-fidelity model is substantially longer than that of the other two models. In contrast, the computational times of the sparse identification model and the 4 DOF dynamic model are comparable and relatively short. It implies that, due to its high complexity and large computational load,

https://doi.org/10.1017/aer.2025.10078 Published online by Cambridge University Press

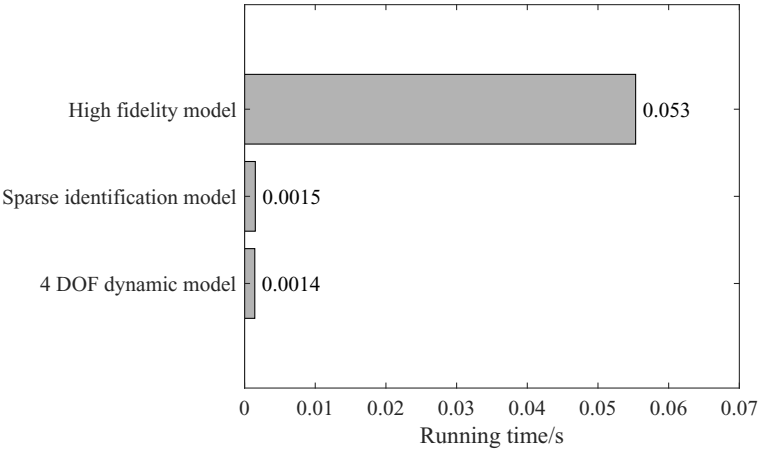


Figure 8. *The average running time of 1,000 simulations for different models.*

the high-fidelity model is ill-suited for the rapid design demands of parafoil path planning. Conversely, the other two models exhibit distinct advantages in computational efficiency and are more appropriate for path planning scenarios with high real-time requirements, which is consistent with the findings of previous research.

5.2.2 Computational accuracy evaluation

Based on the flight test data of a certain type of parafoil system, a detailed comparison was made between the simulated values and the experimental values. A total of four airdrop tests were carried out for this type of parafoil system, and the third typical flight data was selected for model validation. The reason is that the wind field uncertainty of this group of tests is relatively low, which is suitable for verifying the model accuracy. In the test, all sensors were calibrated by the factory and time – synchronised through a 4Hz hardware trigger synchronisation mechanism. After using the Kalman filter to remove noise and outliers, the filtered data was resampled at 10Hz to calculate the RMSE.

The computational accuracy of different models was further evaluated. Figure 9(a) shows the contrast curve of the horizontal position trajectory of the parafoil system, Fig. 9(b) shows the contrast curve of the system height varying with time and Fig. 9(c) shows the contrast curve of the parafoil yaw angle varying with time. Overall, the simulation results of the models are generally in line with the trend of the test values, demonstrating a high degree of coincidence.

The models were further analysed quantitatively. Specifically, the statistical results of the mean error (ME) and RMSE were derived for the sparse recognition model and the 4 DOF dynamic model, which is most prevalently utilised in path planning, in comparison with the test values. The results are presented in Table 3.

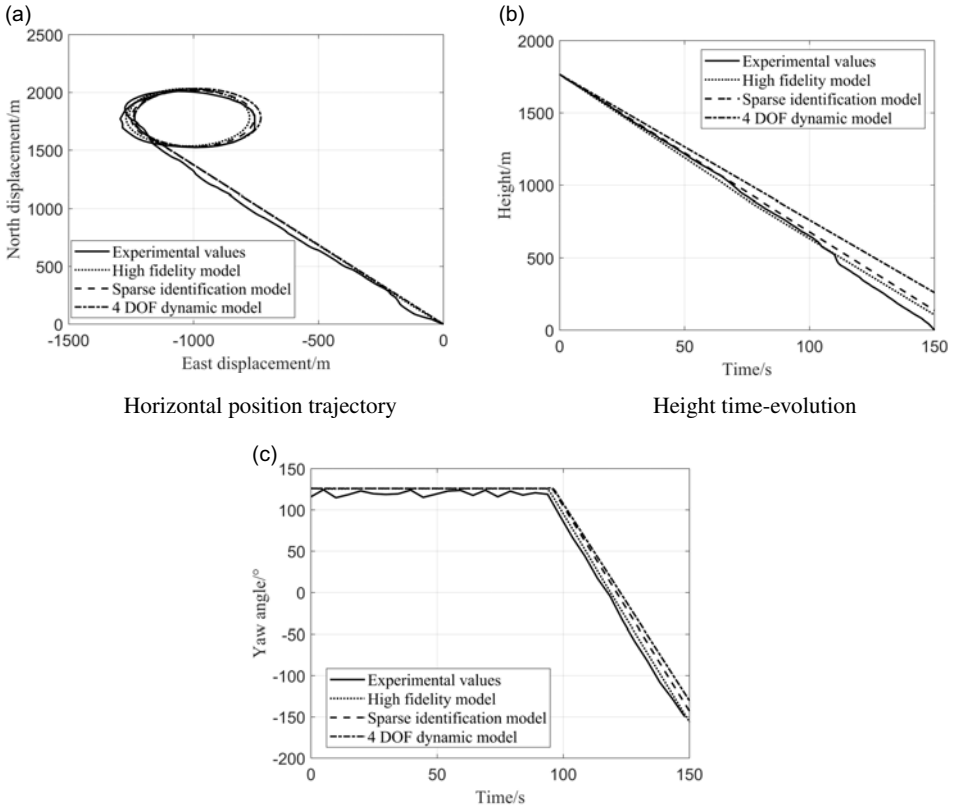
The ME provides an intuitive indication of the overall deviation, both in terms of direction and magnitude, between the model's predicted values and the actual values. It serves as a preliminary assessment of the model's accuracy. As can be seen from the results, regardless of whether it is the error in horizontal position, altitude or yaw angle, the sparse identification model outperforms the 4 DOF dynamic model.

The RMSE comprehensively considers the magnitude and distribution of errors, reflecting the model's precision and stability, and is an effective indicator for comparing model performance. In terms of horizontal displacement, height and yaw angle, the RMSE sparse recognition model is significantly better than the 4 DOF model, which indicates that the accuracy of measurement or calculation is improved.

https://doi.org/10.1017/aer.2025.10078 Published online by Cambridge University Press

Table 3. *Error comparison and reduction rates*

State	Error Type	Error Value		Reduction [%]
		Sparse identification model	4 DOF Dynamic Model	
Horizontal	ME [m]	**15.0511**	15.5181	3.00
Position	RMSE [m]	**56.5410**	64.9617	12.96
	ME [m]	**39.1224**	100.7134	61.15
Height	RMSE [m]	**57.4421**	126.1038	54.44
Yaw angle	ME [°]	**12.9401**	19.2917	32.92
	RMSE [°]	**14.7157**	23.7214	37.96



Horizontal position trajectory

Height time-evolution

Yaw angle time-evolution

Figure 9. *Dynamic model validation: Experimental Data vs. Model Prediction.*

Based on the analysis of running time, it can be concluded that the high-fidelity model is not suitable for rapid trajectory planning design. The proposed sparse identification model significantly outperforms the conventional 4 DOF dynamic model in predictive accuracy, with remarkable RMSE reductions of 12.96% (horizontal position), 54.44% (height) and 37.96% (yaw angle) in trajectory prediction. Combining enhanced accuracy and model simplicity, it is particularly suitable for path planning applications requiring both computational efficiency and high precision.

5.3 Parafoil path planning using sparse identification model

To validate the practical application of the sparse identification model in the path planning task, an optimal control algorithm for the parafoil system is designed. Subsequently, fixed-point path planning of the parafoil is executed under diverse initial conditions.

https://doi.org/10.1017/aer.2025.10078 Published online by Cambridge University Press

5.3.1 Path planning description

The path planning problem of the parafoil system essentially aims to find a path from the deployment point to the target point, subject to specific constraint conditions and achieving specific performance indicators. (The path planning problem for the parafoil system essentially involves determining a route from the deployment point to the target point, while adhering to specific constraints and achieving desired performance metrics.) It can be formulated as the following optimisation problem:

Given the initial and terminal moments t_0 and t_f, the objective is to find the manipulation control function $u(t)$ that minimises the following performance function:

$$J = F(\boldsymbol{x}_0, t_0; \boldsymbol{x}_f, t_f). \tag{26}$$

Meanwhile, the parafoil dynamic equations and the terminal constraints for landing must be satisfied.

$$\dot{\boldsymbol{x}}(t) = f(\boldsymbol{x}(t), \boldsymbol{u}(t)), t \in [t_0, t_f], \tag{27}$$

$$\boldsymbol{G}(\boldsymbol{x}_0, t_0; \boldsymbol{x}_f, t_f) = 0. \tag{28}$$

For programming and calculation convenience, the time interval is normalised. Let

$$\tau = (t - t_0)/(t_f - t_0). \tag{29}$$

Here, $\tau \in [0, 1]$.

After the transformation, Equation (26–29) can be converted into

$$J = F(\boldsymbol{x}_0, 0; \boldsymbol{x}_f, 1), \tag{30}$$

$$\boldsymbol{x}(\tau) = \Delta t f(\boldsymbol{x}(\tau), \boldsymbol{u}(\tau)), \tau \in [0,1], \tag{31}$$

$$\boldsymbol{G}(\boldsymbol{x}_0, 0; \boldsymbol{x}_f, 1) = 0, \tag{32}$$

the discrete time step is defined as $\Delta t = t_f - t_0$.

In the path planning algorithm presented in this paper, the control variables are used to construct the performance index function, that is

$$J = \int_0^{t_f} \left(|\delta_s|^2\right) dt, \tag{33}$$

where t_f represents the landing time of the parafoil, δ_s is the symmetric trailing edge deflections of the parafoil, $\delta_s = 0.5(\delta_r + \delta_l)$.

In this paper, a discretisation method based on Lagrangian polynomial interpolation is adopted to solve the path planning problem, and the classical fourth-order Runge-Kutta algorithm is applied for the integral operation [46, 47]. For the described nonlinear programming problem, the Sequential Quadratic Programming (SQP) algorithm can be used for the solution. Since this method is quite commonly used, its detailed description will not be repeated here.

5.3.2 Path planning result

A path planning simulation is conducted for the sparse identification model. The parameters of the parafoil are shown in Table 1. The initial conditions for the simulation are set as follows:

(1) **Target points**: Assume that its position is the zero point in the northeast-up coordinate system, that is, (0, 0, 0) m.

(2) **Deployment points**: The airdrops are carried out at altitudes of 2,000 meters, 3,000 meters and 4,000 meters, respectively, and the position coordinates are taken as (1,200, 1,000, 2,000) m, (2,200, 1,500, 3,000) m and (3,200, 2,000, 4,000) m, respectively.

Figure 10 shows the three-dimensional trajectories obtained with the optimal control method under different airdrop release conditions; Fig. 11 shows the optimal yaw angles.

https://doi.org/10.1017/aer.2025.10078 Published online by Cambridge University Press

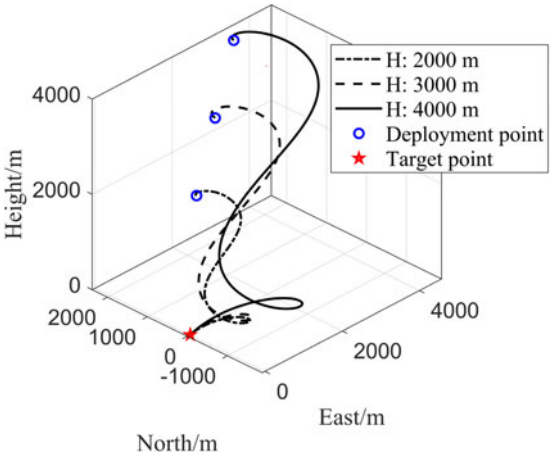


Figure 10. *Comparative analysis of 3D flight path under varying deployment points.*

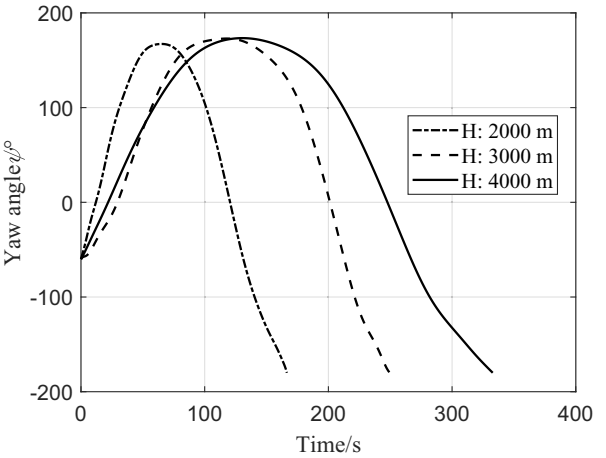


Figure 11. *Optimal yaw angle mapping for different planned path.*

The simulation results show that at the three altitudes, the landing time of the system is about 166.4 s, 249.7 s and 332.9 s, respectively. When the deployment altitude is low, the system does not have enough time to use up the remaining altitude, resulting in a relatively large yaw angle. This behaviour aligns with the actual operation of the parafoil system, confirming that the sparse identification model can accurately describe the movement characteristics of the parafoil. In addition, even though the differences in airdrop release conditions, the approximate model can still be effectively used to plan the flight path to the desired target point according to the requirements. This indicates that the approximate model is well-suited for parafoil path planning and achieves the expected results.

6.0 Conclusion

The parafoil system is a typical multi-flexible body dynamic system, and the modelling of low-order approximate models for path planning has always been a great challenge. This paper explores the sparse identification of the parafoil system. A low-order sparse identification model is identified from high-fidelity data. Then, based on the sparse identification model, the traditional optimal control method

https://doi.org/10.1017/aer.2025.10078 Published online by Cambridge University Press

is used to conduct a path planning simulation of the parafoil system, and the following preliminary conclusions are obtained:

(1) By adopting a data-driven strategy, the SINDyc method suitable for the sparse identification model of the parafoil system was proposed. The simulation results indicate that the initial data volume of the sparse identification affects the accuracy of the identified model. The larger the data volume, the higher the accuracy of the identified model. Compared with the conventional 4 DOF dynamic model, the RMSE in horizontal position, height and yaw angle prediction are reduced by approximately 12.96%, 54.44% and 37.96%, respectively.

(2) The feasibility of applying the sparse identification model to path planning was verified. This research provides a new method for the path planning modelling of the controllable parafoil system. The key parameters of the model are data-driven, which is more universal than the traditional method relying on engineering tests to obtain key parameters.

(3) In terms of algorithm improvement, the currently proposed method requires numerical simulation results as the historical data set for sparse identification. Considering the computational requirements for model accuracy in the path planning of the parafoil system, future work will involve combining experimental data, high-fidelity simulation data and other sources to develop an enhanced algorithm. This algorithm will integrate multi-source and multi-scale data, aiming to further improve the model's accuracy. Beyond the stable operating conditions tested, parafoil path planning must address uncertain scenarios, including wind field disturbances, system parameter perturbations. For instance, sudden payload changes may violate the model's linearised dynamics assumptions, causing planned path drift; insufficient controller bandwidth may allow uncompensated crosswinds to induce path deviation. The sparse structure of our model offers inherent advantages for rapid online trajectory updates, and we will advance algorithm validation under failure modes in subsequent work.

Acknowledgements. This research is funded by the National Natural Science Foundation of China (11772353).

Competing interests. The authors declare no conflict of interest.

References

[1] Stein, J.M. and Madsen, C.M. An overview of the guided parafoil system derived from X - 38 experience, In 18th AIAA Aerodynamic Decelerator Systems Technology Conference and Seminar, Munich, Germany, 2005.
[2] Stein, J.M. Parachute testing for the NASA X-38 crew return vehicle, In 36th Annual International Symposium of Society of Flight Test Engineers, Texas, USA, 2005.
[3] Wang, L.W., Xu W.J., Liu T., Teng H.S., Wu Z. and Liu J.L. Development and prospect of parafoil precise recovery technology for spacecraft, *Spacecr. Recov. Remote Sens.*, 2020, **41**, (4), pp 21–30.
[4] Zhang, X.J. A study of landing flare manoeuvre performance of controllable parafoil system for spacecraft recovery, *J. Natl. Univ. Def. Technol.*, 1996, **18**, (2), pp 9–13.
[5] Goodrick, T. Theoretical study of the longitudinal stability of high-performance gliding airdrop systems, In 5th Aerodynamic Deceleration Systems Conference, Albuquerque, USA, 1975.
[6] Jann, T., Doherr, K.F. and Gockel W. Parafoil test vehicle ALEX. further development and flight test results, In *15th Aerodynamic Decelerator Systems Technology Conference,* Toulouse, France, 1999.
[7] Qin, Y.Z. and Ge Y.J. Preliminary simulation of flight turn performance of controllable parafoil systems, *J. Astronaut.*, 1993, **14**, (1), pp 89–96.
[8] Xiong, J., Song X.M. and Qin Z.Z. Analysis on two body relative movement of parafoil system, *Spacecr. Recov. Remote Sens.*, 2004, **25**, (2), pp 10–17.
[9] Slegers, N. and Costello, M. Aspects of control for a parafoil and payload system, *J. Guid. Control Dyn.*, 2003, **26**, (6), pp 898–905.
[10] Prakash, O. and Ananthkrishnan, N. modelling and simulation of 9-DOF parafoil-payload system flight dynamics, In AIAA Atmospheric Flight Mechanics Conference and Exhibit, Keystone, Colorado, 2006.
[11] Ma, H.L. and Qin, Z.Z. 9-dof simulation of controllable parafoil system for gliding and stability, *J. Natl. Univ. Def. Technol.*, 1994, **16**, (2), pp 49–54.
[12] Vishniak, A. Simulation of the payload-parachute-wing system flight dynamics, In Proceedings of the Aerospace Design Conference, Irvine, USA, 1993.

https://doi.org/10.1017/aer.2025.10078 Published online by Cambridge University Press

[13] Yang, H.P. and He, W.L. Modeling and simulation of 15-DOF parafoil dynamics, *Spacecr. Recov. Remote Sens.*, 2018, **39**, (1), pp 45–52.

[14] Zhang, Q.B., Gao, F., Guo, R., Feng, Z.W. and Ge, J.Q. Multibody dynamics modelling of powered parafoil system using equations with quasi-coordinate, *Acta ArmamentarII*, 2019, **40**, (9), pp 1935–1942.

[15] Li, Z.H., Nan, Y. and Wan, J.C. Research on parafoil path planning based on the original natural algorithm, *Ship Electron. Eng*, 2024, **44**, (3), pp 31–36.

[16] Li, Z.H. and Nan, Y. Optimal path planning and tracking control methods for parafoil, *Appl. Sci-Basel*, 2023, **13**, (14), pp 8115.

[17] Brunton, S.L. and Kutz, J.N. *Data Driven Science and Engineering: Machine Learning, Dynamical Systems, and Control* (2nd ed.), Cambridge: Cambridge University Press, 2022.

[18] Liao, X.F. and Zeng, X.F. Review of target detection algorithm based on deep learning, In *2020 International Conference on Artificial Intelligence and Communication Technology (AICT 2020)*, Guangzhou, Guangdong, 2020.

[19] Raissi, M., Perdikaris, P. and Karniadakis, G.E. Physics-informed neural networks: a deep learning framework for solving forward and inverse problems involving nonlinear partial differential equations, *J. Comput. Phys.*, 2019, **378**, pp 686–707.

[20] Kaptanoglu, A.A., Callaham, J.L., Aravkin, A., Hansen, C.J. and Brunton, S.L. Promoting global stability in data-driven models of quadratic nonlinear dynamics, *Phys. Rev. Fluids*, 2021, **6**, (9), pp 094401.

[21] Sun, Y.H., Li, G.T. and Zhang, G. A satellite anomaly detection method based on distance correlation coefficient and GPR model, *J. Beijing Univ. Aeronaut. Astronaut.*, 2021, **47**, (7), pp 844–852.

[22] Kim, H., Chang, H. and Shim, H. Evaluating MR-GPR and MR-NN: an exploration of data-driven control methods for nonlinear systems, *Int. J. Control Autom. Syst.*, 2024, **22**, (9), pp 2934–2941.

[23] Bongard, J. and Lipson, H. Automated reverse engineering of nonlinear dynamical systems, *Proc Natl Acad Sci U S A*, 2007, **104**, (24), pp 9943–9948.

[24] Schmidt, M. and Lipson, H. Distilling free-form natural laws from experimental data, *Science*, 2009, **324**, pp 81–85.

[25] Brunton, S.L., Proctor, J.L. and Kutz, J.N. Discovering governing equations from data by sparse identification of nonlinear dynamical systems, *Proc. Natl. Acad. Sci.*, 2016, **113**, (15), pp 3932–3937.

[26] Brunton, S.L., Proctor, J.L. and Kutz, J.N. Sparse identification of nonlinear dynamics with control (SINDYc), *IFAC - PapersOnLine*, 2016, **49**, (18), pp 710–715.

[27] Kaiser, E., Kuta, J.N. and Brunton, S.L. Sparse identification of nonlinear dynamics for model predictive control in the low-data limit, *Proc. R. Soc. A*, 2018, **474**, (2219), pp 20180335.

[28] Chu, H.K. and Hayashibe, M. Discovering interpretable dynamics by sparsity promotion on energy and the lagrangian, *IEEE Rob. Autom. Lett.*, 2020, **5**, (2), pp 2154–2160.

[29] Kaheman, K., Kutz, J.N. and Brunton, S.L. SINDy-PI: a robust algorithm for parallel implicit sparse identification of nonlinear dynamics, *Proc. R. Soc. A*, 2020, **476**, (2242), 20200279.

[30] Li, H., Wang, Z. and Wang, W. A local sparse screening identification algorithm with applications, *Comput. model. Eng. Sci.*, 2020, **124**, (2), pp 765–782.

[31] Li, H. *Local Sparse Screening Identification Algorithm of Nonlinear Systems and its Applications* [Dissertation], Tianjin University, Tianjin, 2020.

[32] Li, J.C. *Data Driven Modelling and Analysis of a Type Vibration Energy Harvester Based on Equivalent Linearization* [Dissertation], Tianjin University, Tianjin, 2021.

[33] Conti, P., Gobat, G., Fresca, S., Manzoni, A. and Frangi, A. Reduced order modeling of parametrized systems through autoencoders and sindy approach: continuation of periodic solutions, *Comput. Methods Appl. Mech. Eng*, 2023, **411**, pp 114772.

[34] Fukami, K., Murata, T., Zhang, K. and Fukagata, K. Sparse identification of nonlinear dynamics with low dimensionalized flow representations, *J. Fluid Mech.*, 2021, **926**, p 10.

[35] Fries, W.D., He, X. and Choi, Y. Lasdi: parametric latent space dynamics identification, *Comput. Methods Appl. Mech. Eng*, 2022, **399**, pp 114236.

[36] Callaham, J.L., Brunton, S.L. and Loiseau, J.-C. On the role of nonlinear correlations in reduced-order modelling, *J. Fluid Mech.*, 2022, **938**, p 1.

[37] Prokop, B., Frolov, N. and Gelens, L. Enhancing model identification with SINDy via nullcline reconstruction, *Chaos*, 2024, **34**, (6), pp 063135.

[38] Guevara, B.S., Varela-Aldás, J., Gandolfo, D.C. and Toibero, J.M. SINDy and PD-based UAV dynamics identification for MPC, *Drones*, 2025, **9**, (1), p 71.

[39] Wanner, M. Koopman operators and system identification for stochastic systems [Dissertation], ProQuest Dissertations and Theses Global, 2023.

[40] Rudy, S.H., Brunton, S.L., Proctor, J.L. and Kutz, J.N. Data-driven discovery of partial differential equations, *Sci Adv*, 2017, **3**, p e1602614.

[41] Sha, Y.Y. *Study on Flow Field Characteristics of Tandem Double Cylinders Based on Mode Decomposition Methods* [Dissertation], Harbin Institute of Technology, Harbin, 2021.

[42] Loisseau, J.C., Noack, B.R. and Brunton, S.L. Sparse reduced order modelling: sensor - based dynamics to full - state estimation, *J. Fluid Mech.*, 2018, **844**, pp 459–490.

[43] Li, S.W., Kaiser, E., Laima, S.J., Li, H., Brunton, S.L. and Kutz, J.N. Discovering time varying aerodynamics of a prototype bridge by sparse identification of nonlinear dynamical systems, *Phy. Rev. E*, 2019, **100**, (2), p 022220.

[44] Reza, S.K., John, J. and Di, W. On SINDy approach to measure-based detection of nonlinear energy flows in power grids with high penetration inverter-based renewables, *Energies*, 2024, **17**, (3), 711.

https://doi.org/10.1017/aer.2025.10078 Published online by Cambridge University Press

[45] Yakimenko, O.A. *Precision Aerial Delivery Systems: Modelling, Dynamics, And Control*, American Institute of Aeronautics and Astronautics Inc, 2015, Reston VA.
[46] Conway, B. Practical methods for optimal control using nonlinear programming(Book), *SIAM Rev.*, 2002, **44**, (4), p 714.
[47] Hager, W.W. Runge-Kutta methods in optimal control and the transformed adjoint system, *Numer. Math.*, 2000, **87**, pp 247–282.

Cite this article: Cui Z., Zou W., Feng Z., Zhang Q. and Yang T.. (2026). Sparse identification of parafoil dynamics model for path planning. *The Aeronautical Journal*, **130**, 464–484. https://doi.org/10.1017/aer.2025.10078

https://doi.org/10.1017/aer.2025.10078 Published online by Cambridge University Press